Diamond membrane surface after ion-implantation-induced graphitization for graphite removal: Molecular dynamics simulation

Amihai Silverman
Taub Computer Center, Technion-IIT, Haifa 32000, Israel

Joan Adler
Department of Physics, Technion-IIT, Haifa 32000, Israel

Rafi Kalish
Department of Physics and Solid State Institute, Technion-IIT, Haifa 32000, Israel

(Received 14 February 2011; revised manuscript received 8 May 2011; published 28 June 2011)

Fabrication of diamond membranes, wherein photonic crystals and other nanosized optical devices can be realized, is of great importance. Many spintronic devices are based on specific optically active atomic structures in diamond, such as the nitrogen-vacancy center, and rely on the membrane's performance. One promising approach for realizing such membranes is by creating a heavily damaged layer (rich in broken bonds) in diamond by ion implantation. Following annealing, this layer converts to graphite, which can be chemically removed, leaving a free-standing diamond membrane. Unfortunately, the optical properties of the exposed diamond surface (the diamond-vacuum interface) of such membranes currently are insufficient for high-quality photonic devices. We present molecular dynamics studies of the atomic structure of the etchable graphite/diamond interface. Different implantation and annealing conditions are simulated. The results show that cold implantation, followed by high-temperature annealing ($>1500\,^{\circ}$C) leads to the creation of the sharpest diamond-etchable graphite interface, which should exhibit optimal optical properties among diamond membranes created by the implantation/graphitization method.

DOI: 10.1103/PhysRevB.83.224206 PACS number(s): 07.05.Tp, 31.15.xv, 81.05.uj, 68.35.Ct

I. INTRODUCTION

There is great interest in manipulating and guiding single photons in microsized diamond structures. This is because they are important for developing potential applications of single-photon emitters in diamond as qubits and other building blocks for various quantum devices.[1] The photons require an emission source. One of the most promising centers for emitting such photons, exhibiting the required properties, is the negatively charged nitrogen-vacancy defect center in diamond.[2] Obviously, the optimal material to transport these photons is diamond itself, since it has unsurpassed optical and mechanical properties and the emitting center is naturally embedded therein. In order to achieve this goal, diamond membranes need to be formed with submicrometer thicknesses wherein photonic crystals can be realized. Such a membrane should have optimal optical properties (high transparency and edge reflectivity) to allow undisrupted photon transfer through it and to be of some 200 nm thickness (comparable to the wavelength of the emitted photon in diamond).

The diamond membranes are commonly realized by taking advantage of the fact that heavily damaged diamond, following annealing, tends to convert to etchable graphite.[3] A damaged diamond layer, rich in broken bonds, is created at the required depth by ion implantation. High-temperature annealing is then carried out to convert those regions of the damaged diamond, in which the density of broken bonds exceeds a certain value, to graphite. Regions in front (below in our figures) and beyond (above in our figures) the main damage peak (in which the majority of carbon atoms remain sp^3 bonded) will anneal back to diamond.[4] The graphitized layer can be etched away by applying chemical or electrochemical methods leaving a diamond membrane (the thickness of which is determined by the implantation conditions) that can be lifted off from the substrate and in which the desired optical structure, such as photonic crystals, can be realized. This procedure, when combined with focused ion-beam processing of selected spots in the membrane, has yielded promising optical devices.[5]

Unfortunately, the performance of such devices is, as yet, unsatisfactory. This is possibly because the optical quality of the diamond-vacuum interface following ion-beam-induced graphitization and graphite removal is nonideal. Therefore, it appears that application of the current ion-implantation/graphitization methods do not yield the optical qualities that would enable the utilization of such lift-off methods to obtain high-quality waveguides and other nanosized optical devices.

Thus, understanding the properties of this interfacial layer and finding ways to minimize its detrimental effects on the reflectivity of photons impinging from within the membrane are of major importance. Some laboratory studies along these lines have recently been performed.[6] The structure of the exposed diamond surface following graphite etching has been measured by grazing-angle ion-channeling experiments. Information on the perfection of the very first atomic layers of the exposed diamond surface and which treatments to this surface can improve its quality has been obtained.

We present results of computer simulations of the evolution of graphite and diamond in a diamond sample exposed to carbon-ion implantations resulting in damage to the sample. On annealing, some initially damaged regions regrow as diamond, whereas, the regions that contain a high density of broken bonds result in a graphitic layer within the diamond sample. Since graphite contains carbon atoms with a

three-fold-coordinated sp^2 hybridization, whereas, the carbon atoms of diamond are fourfold coordinated with an sp^3 hybridization, the numbers of sp^2- and sp^3-bonded carbon atoms can accurately be determined at any desired location of the sample. The sharpness of the boundary between the regions of recovered diamond and graphite can thereby be evaluated. In Sec. II, we review general aspects of simulating diamond/graphite transitions. In Sec. III, we present details of our molecular dynamics (MD) simulations. These mimic the damage created by ion implantation more closely than the commonly used stopping and range of ions in matter (SRIM)[7] simulation. The latter implant, i.e., shoots ions into the same spot, each time into an undamaged diamond sample, which is assumed to be amorphous.[7] Our procedure implants atoms sequentially into an initially crystalline, but progressively more locally disturbed, region. Following our implantation process, we expose the damaged sample to different annealing conditions in the computer. As will be described in Sec. IV, by following the distribution of sp^2- and sp^3-bonded carbon atoms before and after the annealing, the regrowth of the damaged layer can be studied. This yields information on the sharpness of the diamond/graphite interface and its dependence on implantation-annealing conditions as presented in Sec. V. In the final Sec. VI, we discuss our results and give guidelines for the optimal experimental conditions to yield the best diamond membrane for optical applications.

II. DIAMOND/GRAPHITE TRANSFORMATION

Diamond and graphite are allotropes of carbon, that is, they have the same building block, namely, the element carbon, but with different atomic hybrid configurations, sp^3 (tetragonal), sp^2 (trigonal), or sp (diagonal). These allotropic solids can be classified into three major categories: (i) the sp^3-structured bulk, which includes diamonds, tetrahedral amorphous carbon, diamondlike carbon, and lonsdaleite, (ii) the sp^2-structured bulk, which mainly includes two-dimensional graphitic planes (graphene) and sp^2-bonded amorphous carbon, and (iii) the fullerenes, such as nanotubes, which are sp^2 hybrids but contain only a few layers or buckeyballs. The sp^2 bonding of carbon atoms is the thermodynamically stable configuration at standard temperature and pressure. However, due to the very high potential barrier between the sp^2- and sp^3-bonding configurations, the sp^3 region is, in practice, stable, unless disrupted by bond breakage and allowed to relax (by thermal annealing) to the most stable sp^2 configuration.

Transformations between diamond (sp^3) and graphite (sp^2) allotropes of carbon have been modeled in a long-term Technion project of computational/experimental comparisons. In our earliest calculations, we modeled the transformation of diamond to graphite under irradiation and viewed the creation of split interstitial defects[8] and the graphitization of local regions in diamond.[9] In more recent projects, we studied the evolution of damage along an ion track in diamond[10] and modeled the formation of nanodiamond and nanographite.[11,12] Together with an excellent success rate of growth and identification of nanodiamonds, a rather surprising result of the computations was the prediction of nanographite formation[12] in the case of slow cooling, which was experimentally confirmed.

Throughout most of these calculations, we based decisions about local carbon hybridization on geometric information regarding the structure of the bonds, such as the number of neighbors, bond lengths, and angles. We used our AViz (Refs. 13 and 14) software to draw differently coordinated atoms and different bond lengths in color to support our visual deductions beyond the decisions based on statistical evaluations. Cross comparison with experimental results has led to a high level of confidence in our deductions.[8–10] However, a direct comparison of the geometrical structure with the nature of the local electronic density of states would give even better support. Most recently, we were able to study this density for the cases of different carbon-bonding configurations[15] with the use of the Vienna *ab initio* simulation package code (VASP).[16,17] We observed that the shorter bond of the split interstitial, where both atoms are sp^2 hybridized, indeed has a charge distribution reminiscent of that of graphite between two adjacent carbon atoms. The bonds between adjacent sp^3-hybridized atoms of diamond showed different, also distinctive, charge distributions. While this detailed electronic density characterization is only possible for very small samples, its implications are also useful for larger samples. Having obtained this long-sought confirmation that our geometrical characterizations do indeed also correctly estimate the chemical nature of the hybridizations, we can continue, with confidence, to the present paper. Here, we simulate the bonding configuration of carbon atoms in a diamond matrix that has been subjected to different bond breaking (implantation damage) and thermal treatments (annealing) and infer from them the chemical etchablity of the various regions in the disrupted diamond sample.

III. THE SIMULATION METHOD

A. The interatomic potentials

The reactive empirical bond order (REBO) potential, which is an empirical many-body classical potential, was used in the MD simulations. The potential was developed by Brenner,[18,19] and it is based on potentials introduced and parametrized by Abell[20] and Tersoff.[21] The parameters in this potential are empirically derived by fitting to data sets from both experiments and *ab initio* calculations. Hence, this potential does not treat electrons explicitly nor does it include any explicit quantum effects. The REBO potential was originally developed for use in simulating the chemical vapor deposition of diamond[18] and more recently, has been extended to enable more accurate treatment of the energetic, elastic, and vibrational properties of solid carbon and small hydrocarbons. The potential has also been used to model many different carbon-related structures and processes, including fullerenes,[22,23] carbon nanotubes,[24] amorphous carbon,[25] and graphene,[26] and recently, a new extension was developed for graphene.[27] Thus, it is well suited for simulating the present case of implantation damage (annealing) of diamond.

B. The thermostat

The Langevin dynamics thermostat[28] was used for the isothermal MD simulation. This thermostat was applied in all the tasks involving temperature changes: (i) annealing the

samples at the end of the damaging (implantation) process, (ii) cooling the samples at the end of the damaging and annealing processes to a temperature of 0 K in order to freeze-in the structure for the analysis, and (iii) heating the diamond samples that were used as initial samples in the hot-implantation simulations.

C. The sample geometry

The simulated diamond samples consisted of 5120 carbon atoms initially arranged in a pure diamond structure containing $8 \times 8 \times 10$ unit cells with full periodic boundary conditions. The 8×8-cell planes were in the X-Y direction, and ten cells were in the Z direction. Figure 1 depicts a schematic of the sample where the X, Y, and Z directions are indicated. The lattice is oriented in the (100) direction. We note that, in experiments, the implantations are made through the lowest face of the pictured sample.

D. The damaging (shooting) process

In the ion-implantation experiment, high (MeV) energy atoms are implanted into the sample surface. The interaction cross section of the implanted atoms is at its peak when the implanted atoms' kinetic energy is reduced after the atoms were stopped.[3,8] We simulated the final stage of the implantation-induced damage. At this stage, the kinetic energies of the implanted atoms are reduced to the level of the top interaction cross section. Single carbon atoms were individually shot into the diamond samples by applying the following procedure: A carbon atom was inserted between layers 11 and 12, counting from the bottom of the sample. The location inside the layer (i.e., the X-Y coordinate) was chosen randomly for each carbon atom. An initial velocity, which corresponded to a kinetic energy of 350 eV, was delivered to this atom in a direction 7° away from the Z axis in order to minimize the chance of channeling ions down major crystallographic axes in the diamond structure, see Fig. 1. The dashed lines show the X-Y plane where the carbon atoms are inserted for implantation. The filled circles denote the initial locations (randomly selected) of carbon atoms, and the arrows show the direction of momentum imparted to these atoms, i.e., the implantation direction (θ denotes the 7° angle of implantation). This angle of implantation is commonly selected for laboratory implantations because it avoids any possible channels in the diamond crystal.

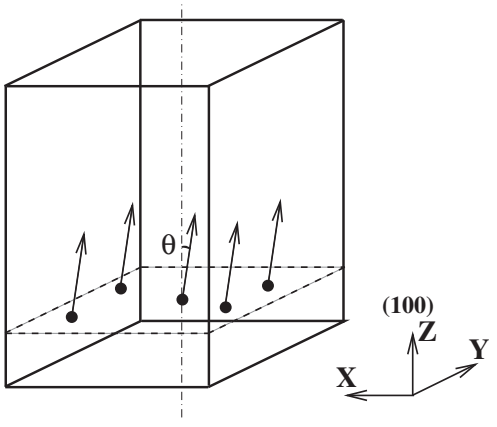

FIG. 1. A schematic of the sample. The dashed lines denote the X-Y plane where the carbon atoms are inserted for implantation. The filled circles and arrows denote the initial locations of carbon atoms and the direction of implantation, respectively. θ denotes the 7° angle of implantation.

This procedure results in the carbon atoms moving inside the sample while displacing host carbon atoms, creating vacancies and interstitials in the diamond crystal in a manner similar to that experienced in actual ion-damage experiments during the final stages of the ion-stopping process.[3,8] At the end of the implantation process, the implanted atoms remain in the sample, hence, the sample periodic boundary conditions are applied to the implanted atoms as well. An energy of 350 eV was chosen for the initial kinetic energy of the implanted atoms. This value was about seven times the displacement energy for carbon atoms in diamond, as obtained in previous simulations.[9] Preliminary runs showed that the damage caused by implanting a carbon atom with this energy extended for about 20 atomic layers, i.e., the damage was confined to the middle of the sample that consisted of 40 layers. In the sequential implantation process, the time for each implanted atom, including the time allowed for sample relaxation, was 100 fs. (For each atomic implantation, the disturbances ended after 80–100 fs, and at the end of this time, the implanted atoms were restrained, and their neighbors were relaxed.) Therefore, the total process of damaging the sample by implanting 20 carbon atoms took 20×100 fs $= 2000$ fs. The cooling to a temperature of 0 K took 2000 fs. Each sample was allowed to relax for another 5000 fs at 0 K before the collection of statistics of the sample in its final configuration.

E. Implantation schedules

In order to investigate the effect that different implantation/annealing procedures may have on the resulting damage, three schedules were modeled. Their stages are illustrated schematically in Fig. 2. Note that, during implantation, kinetic energy is delivered to the entire system, and so its temperature rises slowly. The final cooling processes are rapid, but not instantaneous, quenches.

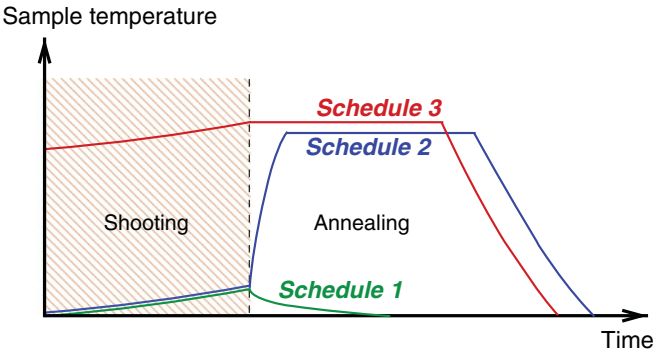

FIG. 2. (Color online) A schematic of the three different schedules, online colors of the schedule curves correspond to data points in some later figures.

1. Schedule 1

Simulation of as-implanted damage:
(i) Initial sample—diamond at a temperature of 0 K,
(ii) damaging by implanting 20 carbon atoms, as described above,
(iii) cooling to 0 K in order to freeze-in the atomic configuration at the end of the damage process.

2. Schedule 2

Simulation of cold implantation followed by annealing:
(i) Initial sample—diamond at a temperature of 0 K,
(ii) damaging by implanting 20 carbon atoms, as described above,
(iii) fast heating followed by annealing at a selected temperature for a time of 8000 fs,
(iv) cooling to 0 K.

3. Schedule 3

Simulation of implantation into a preheated sample (hot implantation):
(i) Initial sample—diamond that was preheated to a selected temperature (preheating not shown in Fig. 2),
(ii) damaging by implanting 20 carbon atoms, as described above,
(iii) annealing at the same selected temperature [(i) above] for 8000 fs,
(iv) cooling to 0 K, which lasted for 2000 fs, followed by another 5000 fs at 0 K. The heating and cooling were achieved by running a MD simulation with a Langevin thermostat.[28] Each MD time step was 1 fs. In order to properly compare the results of the three schedules, the same initial X-Y locations of the inserted/implanted atoms were used for the three schedules. This procedure was repeated several times to allow statistical comparison between several independent implantation-damaging sessions.

F. Statistics

In order to verify the consistency of our results, ten samples of different initial coordinates were prepared. We found that, in addition to the effect of the schedule on the results, different sets of random initial X-Y coordinates for the inserted atoms caused slightly different damage details and, therefore, slightly different damage profiles. Before beginning to compare results of the different schedules, we explored the variation between samples that were identical except for the randomness in the initial selection of shot atoms.

Figure 3 shows the fraction of sp^2 bonds for samples annealed at 2000 °C according to Schedule 2 for five samples having different initial X-Y coordinates. We observe that the distribution of the fraction of sp^2 bonds has a similar peak half-width, but there is some displacement regarding at which layer the damage begins, and the sharpness of the upper part of the peaks varies. However, the area under the curves is very similar. Similar amounts of variation are found for other schedules over different groups of samples. In order not to confuse sample differences with schedule effects, we chose to plot the fraction of sp^2 of the different schedules for each sample separately: In each case, the same initial

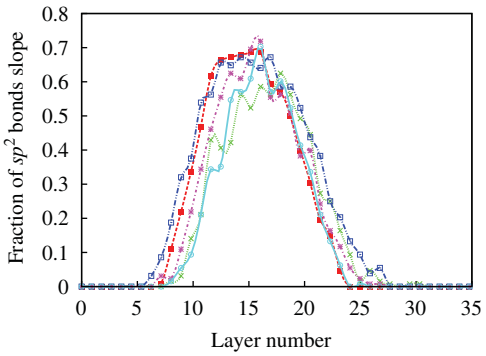

FIG. 3. (Color online) The fraction of sp^2 bonds for samples with different initial X-Y coordinates for the shot atoms, annealed at 2000 °C, according to Schedule 2. Online colors correspond to different samples.

X-Y coordinates were used for all the schedules. We will discuss variations between different samples following the presentation of our comparison between scheduling effects below.

IV. ANALYSIS METHODS

A. Calculations of the fraction of sp^2 bonds

The aim of the present paper is to investigate the sharpness of the diamond/graphitized-damaged-diamond interface following different implantation-annealing schemes. Therefore, the bonding configuration (whether it is predominantly sp^2 or sp^3) of each atom in the sample, following the various procedures, must be obtained. Two methods for deducing this were employed:

1. Method 1: Counting the number of nearest neighbors

In this method, the number of neighbors was calculated for each atom within the first nearest-neighbor distance. Atoms with four neighbors within this radius were assigned to be sp^3 bonded, and atoms with three neighbors were assigned to be sp^2 bonded.

The following stages in the calculation were performed: First, the radial distribution function (RDF) of each layer was calculated, i.e., the RDF was calculated for the bonds of the atoms in layer l, and the calculation was repeated for all 40 layers ($l = 1, \ldots, 40$) in the Z direction. Next, the first-neighbor distance was determined from the location of the first peak in the RDF plot. Then, the number of neighbors within the radial distance of the first neighbor was counted for each atom in layer l. Finally, the ratio (f_{l,sp^2}) between the number of atoms with three neighbors N_{l,sp^2} (sp^2 bonds) and the number of atoms with three and four neighbors $N_{l,sp^2} + N_{l,sp^3}$ was calculated for each layer l as

$$f_{l,sp^2} = \frac{N_{l,sp^2}}{N_{l,sp^2} + N_{l,sp^3}}. \quad (1)$$

This calculation was repeated for each of the implantation-annealing sessions. The results of these were plotted versus the layer number l.

2. Method 2: RDF peak area

An alternative approach for estimating f_{l,sp^2} was also carried out. The length of the carbon sp^2 bond in graphite at 300 K is 1.42 Å, while that of the diamond sp^3 bond is 1.54 Å. The difference in the bond length of the sp^2- and sp^3-bonded carbon atoms in the samples is noticeable as separate peaks in the RDF plots (see Fig. 5). Note that, in the interface and disordered regions, the second peak is typical of a disordered system, and in the diamond region, it is ordered. The RDF of each layer l was calculated separately, and the areas of the sp^2 and sp^3 peaks of each layer were recorded. The ratios between the peak areas were then calculated according to Eq. (1) for each layer l, where, here, N_{l,sp^2} denotes the area of the sp^2-bonds peak, and N_{l,sp^3} denotes the area of the sp^3-bonds peak for layer l. The estimates from this approach for calculating the ratio f_{l,sp^2} were also plotted versus layer number l.

B. The sharpness (slope) of the sp^2-fraction curve

The main purpose of the present paper is to find the implantation-annealing scheme that yields the sharpest interface between the heavily damaged diamond which, following annealing, converts to sp^2-bonded graphite and the undamaged sp^3-bonded diamond regions. In order to compare the sharpness of interfaces of the sample following the different processes, the slopes of the plots of the sp^2 fraction versus the layer number were calculated using a five-point stencil first-derivative algorithm.[29,30] These were plotted versus the layer number, i.e., versus the depth in the sample.

C. The average atomic movement

In order to get an insight into the damage to the sample, after the different implantation-annealing processes, the displacements of each atom in the sample from their initial sites were evaluated, i.e., for each atom, the differences between the coordinates of the original atomic site in the initial sample and the site of the same atom, after the process was completed, were calculated. The root-mean-square movements of all the atoms in layer l were averaged for each of the 40 layers in the Z direction. We noticed that, after the implantation and annealing processes, layers moved as clusters in the Z direction. In order to eliminate this effect, the coordinate differences of the projection on the X-Y plane were considered for this calculation.

V. RESULTS

Below, we present a comprehensive summary of results obtained from one set of initial conditions. As mentioned above, the results, obtained from the nine other identically treated samples (each with different randomly selected initial locations) of the implanted carbons, were rather similar.

Figure 4 depicts a [100] view of a sample produced according to Schedule 2, i.e., 20 carbon atoms were implanted at a temperature of 0 K into the ideal diamond crystal, inflicting damage on it that, subsequently, was annealed at a temperature of 2000 °C and then cooled back down to 0 K (see Figs. 1 and 2). The initial locations of the implanted atoms were from the 11th atomic layer (counted from the bottom of the sample upward). The dark (blue online) lines depict bonds of four-fold- (sp^3)-coordinated atoms, while the light (yellow online) lines depict bonds of three-fold- (sp^2)-coordinated atoms. As can be seen in Fig. 4, the damage and the subsequent annealing have converted most of the atomic bonds in the center of the sample from sp^3-diamond bonds to sp^2-graphite bonds.

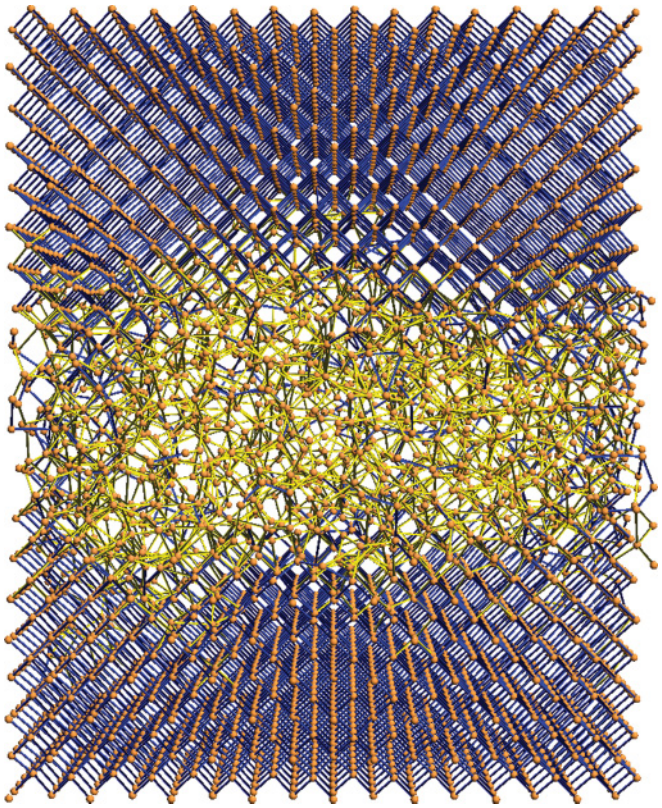

FIG. 4. (Color online) The atomic structure of a sample that was damaged with 20 carbon atoms at 0 K, was annealed at 2000 °C, and then was cooled back to 0 K (Schedule 2). The dark (blue online) lines represent fourfold (sp^3) bonds, and the light (yellow online) lines represent threefold (sp^2) bonds.

Figure 5 shows the RDF of three different layers in a sample that was damaged according to Schedule 2 at a temperature of 0 K, then was annealed at a temperature of 2000 °C, and then cooled back to 0 K. The RDF was calculated separately for the bonds in each X-Y atomic layer. In Fig. 5(a), the RDF is shown for layer number 23, which is in the middle of the damaged region. Two nearest-neighbor peaks are observed, one at 1.42 Å and a smaller one at 1.54 Å. The major peak, at 1.42 Å, is due to carbon atoms with the graphitic sp^2 hybridization, and a minor peak, at 1.54 Å, appears at the diamond sp^3-bond length. Integrating the area below the two peaks yields that 70% of the bonds in the damaged volume are sp^2-bonded carbon atoms. Figure 5(b) displays the RDF calculated for layer number 26, which is in the middle of the interface between the damaged volume and the diamond volume beyond the damaged volume. Two nearest-neighbor peaks of similar heights are observed, one at 1.54 Å due

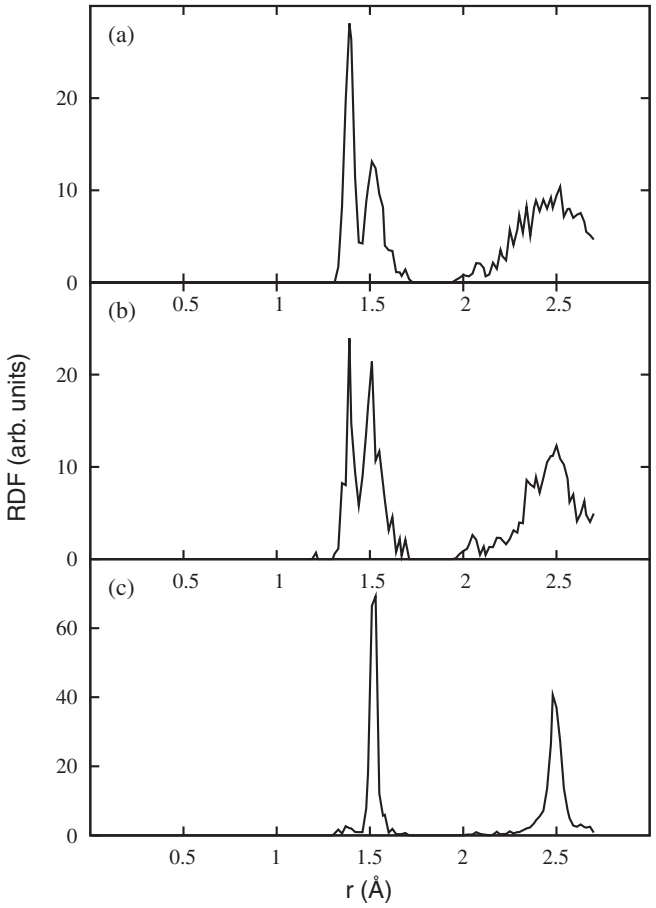

FIG. 5. RDF plots of layer number 23—in the middle of the damaged region (a), layer number 26 in the interface (b), and layer number 30—outside the interface (c). The sample was damaged with 20 carbon atoms at 0 K, was annealed at 2000 °C, and then was cooled to 0 K, Schedule 2.

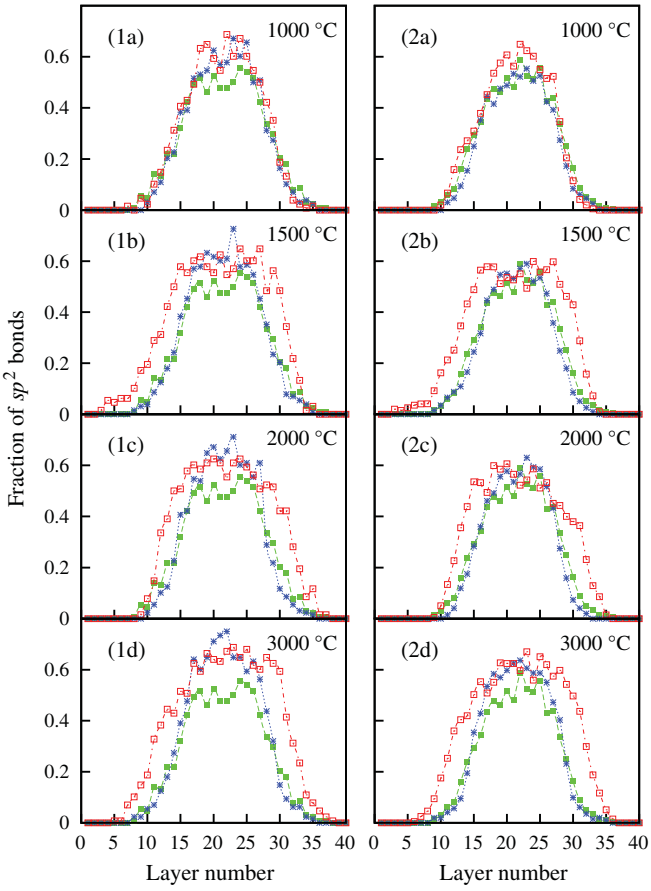

FIG. 6. (Color online) The fraction of sp^2 bonds in different samples subjected to different annealing temperatures. The eight plots show the sp^2 fraction in each layer in a sample, where each plot depicts the three different schedules (see Sec. III). Schedule 1 is depicted by filled squares (green online), Schedule 2 is depicted by asterisks (blue online), and Schedule 3 is depicted by empty squares (red online). The annealing temperatures were 1000 °C for plots (a), 1500 °C for plots (b), 2000 °C for plots (c), and 3000 °C for plots (d). The two columns (1 and 2) represent the same data subjected to different analysis methods, the left-hand column plots were made using Method 1, and the right-hand column plots were made using Method 2.

to the diamond sp^3 bonds and one at 1.42 Å, which is the graphite sp^2-bond length. Figure 5(c) displays the RDF curve for layer number 30, which is beyond the damaged volume. It is dominated by a single nearest-neighbor peak at 1.54 Å due to the pure diamond structure of this layer.

Figure 6 shows the results of the fraction of sp^2 bonds in samples subjected to different annealing temperatures, 1000 °C for plots (a), 1500 °C for plots (b), 2000 °C for plots (c), and 3000 °C for plots (d). Each plot contains the data for the three different implantation-annealing schedules. Schedule 1 is depicted by filled squares (green online), Schedule 2 is depicted by asterisks (blue online), and Schedule 3 is depicted by empty squares (red online). The two columns (1 and 2) represent the same data subjected to different analysis methods, the left-hand column plots were made using Method 1, and the right-hand column plots were made using Method 2 (see Sec. IV above).

Figure 7 depicts the slopes (first derivative relative to the distance along the Z axis) of the concentration of sp^2-bonded carbon atoms implanted and annealed according to Schedule 2 and calculated using Method 1. Each plot represents a different annealing temperature. The results were smoothed using a spline algorithm.[29] It should be noted that the peak of the slopes, i.e., the sharpest change from graphite to diamond is centered on the tailing edge of the implantation profile in layer number 28. The dip in the left-hand side of the figure depicts the sharpness of the interface between the graphitized volume and the nondamaged (recovered) diamond volume, the implantation (annealing), and the scheme that yields the sharpest derivative curve is that which should show the sharpest interface, i.e., the exposed diamond surface with the least residual damage.

Figure 8 shows the average atomic movement of the atoms in the X-Y plane in the various layers implanted according to the three different schedules discussed in Sec. III D: for the as-implanted (Schedule 1) sample, for the same sample annealed at 2000 °C after the cold implantation (Schedule 2), and for a sample implanted hot (at 2000 °C, Schedule 3). The movements of atoms kicked from their initial sites, as a result of the implantation, are projected in the X-Y plane.

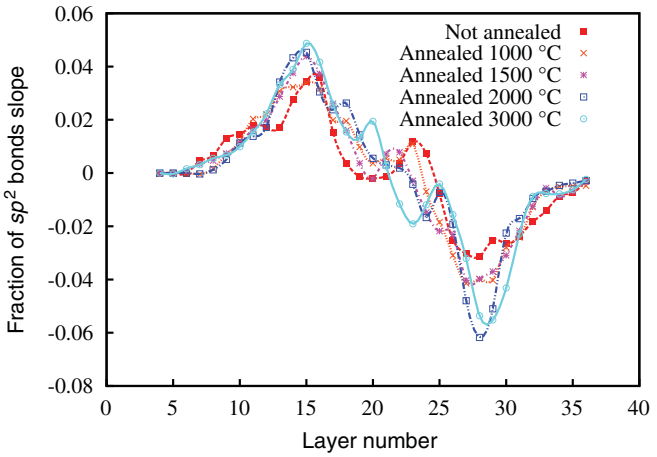

FIG. 7. (Color online) The slope of the sp^2 fraction in each layer for the same sample that was annealed after the implantation at different temperatures with Schedule 2. The dip in the right-hand side of the graph is discussed in depth in the text.

As can be seen, postimplantation annealing does not result in any observable motion of the carbon atoms, whereas, hot implantations result in a very substantial motion of the recoiling atoms in the hot environment.

After this detailed presentation of one set of results, we now consider how to explore the total body of results from the ten different samples. Figures similar to Fig. 6 were prepared for different initial coordinates and, except that the locations in the Z direction of the layers, where the disruption was found, were in slightly different places, the overall situation was similar. The intersample variation was compared with a measure that was equivalent to the total area under the sp^2-fraction curve depicted in Figs. 3 and 6. This measure, the percentage of the sp^2 bonds in the whole sample, is shown in Fig. 9 as

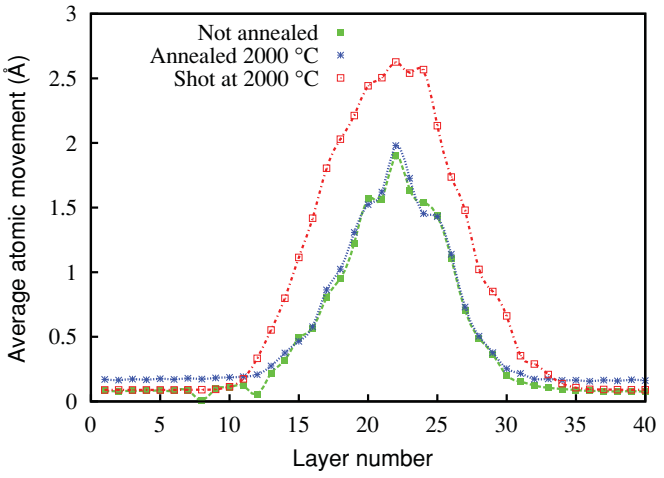

FIG. 8. (Color online) The average atomic movements projected to the X-Y plane of carbon atoms in the different layers for different implantation-annealing schedules. The sample was implanted with 20 carbon atoms. Shown are the movements of the as-implanted sample (at 0 K) (full circles—green), the movements of atoms in the same sample annealed at 2000 °C (stars—blue), and in a sample that was hot implanted (open circles—red).

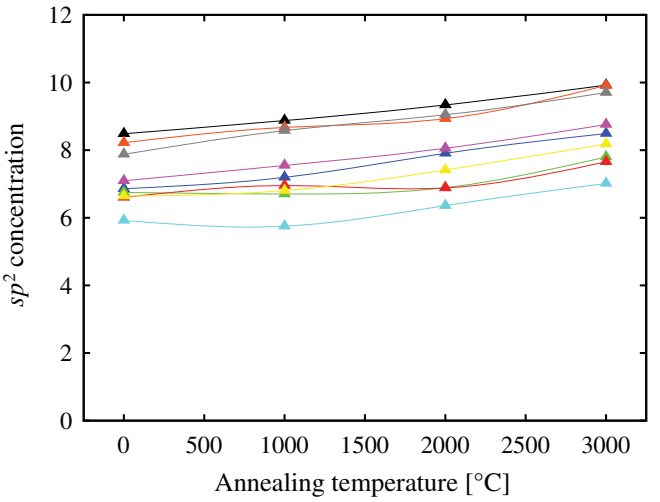

FIG. 9. (Color online) The sp^2-bonds concentration for different samples (each has a different symbol and color online) at 0 K (Schedule 1) and annealed at temperatures of 1000 °C, 2000 °C, and 3000 °C with Schedule 2.

a function of the annealing temperature for different sets of random initial coordinates for the shot atoms. Each line depicts one sample. The point at $T = 0$ represents no annealing after the implantation (Schedule 1, filled green squares in Fig. 6), where the other points depict the results after annealing at 1000 °C, 2000 °C, and 3000 °C, according to Schedule 2. (We remind the reader that the variation between the samples is a different set of random initial coordinates for the shot atoms.) Figure 10 shows the percentage of the sp^2 bonds as in Fig. 9, but now the Y-axis values are scaled so that the plots overlap.

Similar behavior is observed across the samples, as is also observed for other schedules (temperatures). There is a trend of a higher concentration of sp^2 bonds at higher annealing temperatures. Overall, while there is a dependence of damage location on the initial coordinates, there is no consistent observable effect of the measurement method, and these

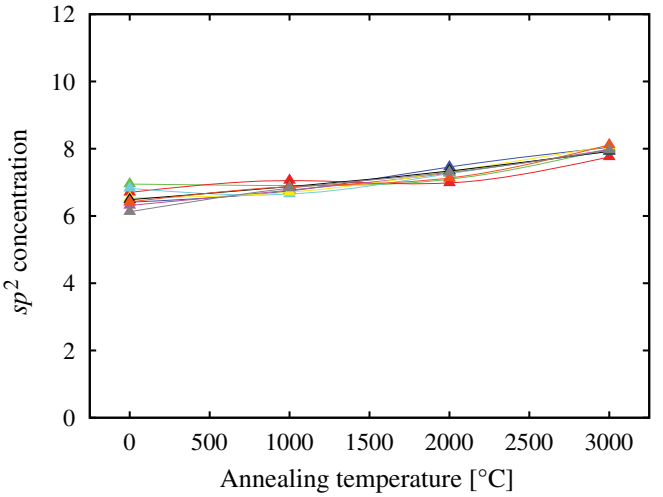

FIG. 10. (Color online) The sp^2-bonds concentration for different samples (each has a different symbol and color online). These are the same data as in Fig. 9 but with rescaled Y-axis values.

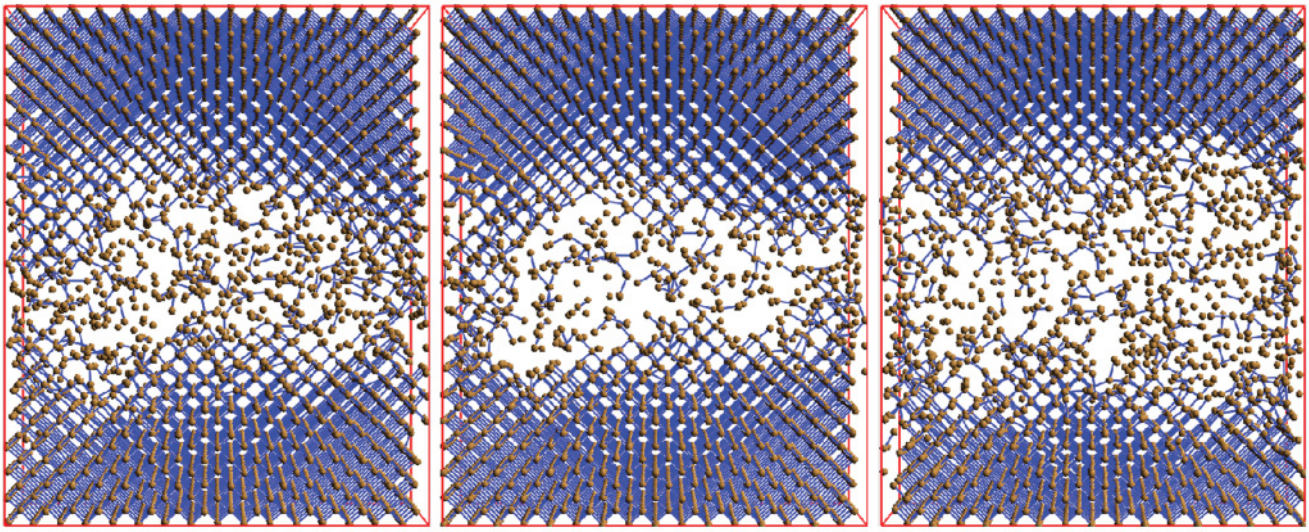

FIG. 11. (Color online) Atomic images of three cases (left to right), prepared with Schedules 1 (as implanted), 2 (cold implantation, annealed at 2000°), and 3 (hot implantation). The center one is the same case as shown in Fig. 4. Rotating images of these figures are given in Ref. 31.

cross-sample comparisons confirm that the data presented in detail are representative of all samples.

Figure 9 emphasizes the variation in the damage profile (depicted as the sp^2-bonds concentration) between samples with different random sets of coordinates for the implanted atoms. This variation is mainly as a result of the small size of our samples relative to the experiment. The variation in the sp^2 concentration from $T = 0\,^{\circ}\mathrm{C}$ to $T = 3000\,^{\circ}\mathrm{C}$ is smaller than the variation in the sp^2 concentration between different samples. We presented the results of Figs. 6–8 for a single sample and not the average results of ten samples with different sets of coordinates for the implanted atoms. Plotting the average results over all the samples causes the differences between the annealing temperatures to vanish.

VI. SUMMARY AND DISCUSSION

The purpose of this paper was to search, by performing computer simulations, for an implantation-annealing scheme for diamond that will lead, after graphite removal, to as sharp a diamond-vacuum interface as possible, as required for photonic device applications. The schedules investigated were as follows: cold implantation with no further annealing, cold implantation followed by annealing at different temperatures, and hot implantations at different temperatures, i.e., implantations into a preheated diamond. From the results presented in Fig. 6, it is clear that annealing at high temperatures of 2000 °C and 3000 °C sharpens the interface, whereas, annealing at lower temperatures (1000 °C and 1500 °C) only causes minor differences to the interface sharpness. These results were compared to the cold implantation (Schedule 1), which did not improve the interface sharpness in any way. Implanting the carbon atoms into a preheated sample (hot implantations) substantially widens the damaged volume but does not make the interface sharper.

These conclusions can be confirmed by directly viewing AViz visualizations of atomistic images following the different implantation schemes (see Fig. 11). This figure shows the atomic images of three cases (left to right), prepared according to Schedule 1 (cold implantation), Schedule 2 (cold implantation followed by high-temperature annealing), and Schedule 3 (hot implantation), see Fig. 2. For clarity, the visualizations were made by only drawing the four-fold-coordinated atoms and the bonds between them and omitting the three-fold-coordinated atoms. Anyway, these would be removed by etching. In that figure, very significant changes between implantation into a cold sample and implantation into a hot sample can be seen (Fig. 11, middle versus Fig. 11, right-hand side). It is reasonable to assume that the totally unsupported fourfold atoms would also be removed in the etching, however, these were not removed in the figures. We observe that the interface between the diamond and the etched regions of a diamond sample prepared by the use of Schedule 3 is wide and messy, while that produced by Schedule 2 is the sharpest. One should also note that implanting into a hot sample causes more atomic disruptions in a larger damaged volume than implanting into a cold sample, hence, the damaged region is not only fuzzier, but it is also larger in the case of hot implantation. The interested reader is referred to our website[31] for rotating images that enable clearer viewing.

In conclusion, damaging diamond with carbon ions (or, possibly also other interstitial/vacancy-producing ions) at low temperatures followed by annealing at as high a temperature as possible should result in the sharpest diamond-vacuum interface of a membrane created by the damage-annealing-graphite removal method.

ACKNOWLEDGMENTS

R.K. acknowledges partial support by the EU (ISF) ERANET Project No. 2127/08 and by the GIF Project No. 1-1026-9.14/2009.

[1]D. D. Awschalom, R. Epstein, and R. Hanson, Sci. Am. **297**, 84 (2007).
[2]J. R. Weber, W. F. Koehl, J. B. Varley, A. Janotti, B. B. Buckley, C. G. V. de Walle, and D. D. Awschalom, Proc. Natl. Acad. Sci. USA **107**, 8513 (2010).
[3]M. S. Dresselhaus and R. Kalish, *Ion Implantation in Diamond, Graphite and Related Materials*, Springer Series in Materials Science, Vol. 22 (Springer-Verlag, Berlin, 1992).
[4]C. Uzan-Saguy, C. Cytermann, R. Brener, V. Richter, M. Shaanan, and R. Kalish, Appl. Phys. Lett. **67**, 1194 (1995).
[5]I. Bayn and J. Salzman, Opt. Express **16**, 4972 (2008).
[6]V. S. Drumm, A. D. C. Alves, K. Ganesan, B. A. Fairchild, J. C. McCallum, D. N. Jamieson, S. Prawer, S. Rubanov, R. Kalish, and L. C. Feldman, Appl. Phys. Lett. **98**, 231904 (2011).
[7]J. F. Ziegler, J. P. Biersack, and M. D. Ziegler, *SRIM, the Stopping and Range of Ions in Matter* (Lulu Press, Morrisville, NC, 2008).
[8]D. Saada, J. Adler, and R. Kalish, Int. J. Mod. Phys. C **9**, 61 (1998).
[9]D. Saada, J. Adler, and R. Kalish, Phys. Rev. B **59**, 6650 (1999).
[10]A. Sorkin, J. Adler, and R. Kalish, Phys. Rev. B **70**, 064110 (2004).
[11]A. Sorkin, J. Adler, and R. Kalish, Phys. Rev. B **74**, 064115 (2006).
[12]A. Sorkin, J. Adler, and R. Kalish, Phys. Rev. B **78**, 155435 (2008).
[13]J. Adler, Comput. Sci. Eng. **5**, 61 (2003).
[14]J. Adler, J. Fox, R. Kalish, T. Mutat, A. Sorkin, and E. Warszawski, Comput. Phys. Commun. **177**, 19 (2007).
[15]J. Adler, J. Zaffran, A. Silverman, A. Sorkin, O. Cohen, and R. Kalish, Comput. Phys. Commun. **182**, 2009 (2011).
[16]G. Kresse and J. Furthmüller, Phys. Rev. B **54**, 11169 (1996).
[17]G. Kresse and D. Joubert, Phys. Rev. B **59**, 1758 (1999).
[18]D. W. Brenner, Phys. Rev. B **42**, 9458 (1990).
[19]D. W. Brenner, Phys. Status Solidi B **217**, 23 (2000).
[20]G. C. Abell, Phys. Rev. B **31**, 6184 (1985).
[21]J. Tersoff, Phys. Rev. Lett. **56**, 632 (1986).
[22]Y. Yamaguchi and S. Maruyama, Chem. Phys. Lett. **286**, 336 (1998).
[23]X. Z. Ke, Z. Y. Zhu, F. S. Zhang, F. Wang, and Z. X. Wang, Chem. Phys. Lett. **313**, 40 (1999).
[24]S. Frankland and D. W. Brenner, Chem. Phys. Lett. **334**, 18 (2001).
[25]S. B. Sinnotta, R. J. Colton, C. T. White, O. A. Shenderova, D. W. Brenner, and J. A. Harrison, J. Vac. Sci. Technol. A **15**, 936 (1997).
[26]Y. Huang, J. Wu, and K. C. Hwang, Phys. Rev. B **74**, 245413 (2006).
[27]V. K. Tewary and B. Yang, Phys. Rev. B **79**, 075442 (2009).
[28]S. A. Adelman and J. Doll, J. Chem. Phys. **64**, 2375 (1976).
[29]William H. Press, Saul A. Teukolsky, William T. Vetterling, and Brian P. Flannery, *Numerical Recipes 3rd Edition, The Art of Scientific Computing* (Cambridge University Press, Cambridge, 2007).
[30]M. Abramowitz and I. A. Stegun, *Handbook of Mathematical Functions with Formulas, Graphs, and Mathematical Tables* (Dover, Mineola, NY, 1970), table 25.2.
[31][http://phycomp.technion.ac.il/∼phr76ja/membrane/membrane-movies.html]